Journal of Alloys and Compounds 480 (2009) 810–819

Contents lists available at ScienceDirect

Journal of Alloys and Compounds

journal homepage: www.elsevier.com/locate/jallcom

Microstructures, mechanical properties and corrosion behavior of high-pressure die-cast Mg–4Al–0.4Mn–*x*Pr (*x* = 1, 2, 4, 6) alloys

Jinghuai Zhang[a,b], Ke Liu[a,b], Daqing Fang[a], Xin Qiu[a], Peng Yu[c], Dingxiang Tang[a], Jian Meng[a,*]

[a] State Key laboratory of Rare Earth Resource Utilization, Changchun Institute of Applied Chemistry, Chinese Academy of Sciences, Changchun, 130022, China
[b] Graduate School of the Chinese Academy of Science, Beijing 100049, China
[c] School of Biological Engineering, Changchun University of Technology, Changchun, 130012, China

ARTICLE INFO

Article history:
Received 12 November 2008
Received in revised form 11 February 2009
Accepted 14 February 2009
Available online 4 March 2009

Keywords:
Mg–Al–Mn–Pr alloy
Microstructure
Mechanical properties
Corrosion

ABSTRACT

Mg–4Al–0.4Mn–*x*Pr (*x* = 1, 2, 4 and 6 wt.%) magnesium alloys were prepared successfully by the high-pressure die-casting technique. The microstructures, mechanical properties, corrosion behavior as well as strengthening mechanism were investigated. The die-cast alloys were mainly composed of small equiaxed dendrites and the matrix. The fine rigid skin region was related to the high cooling rate and the aggregation of alloying elements, such as Pr. With the Pr content increasing, the α-Mg grain sizes were reduced gradually and the amounts of the Al_2Pr phase and $Al_{11}Pr_3$ phase which mainly concentrated along the grain boundaries were increased and the relative volume ratio of above two phases was changed. Considering the performance-price ratio, the Pr content added around 4 wt.% was suitable to obtain the optimal mechanical properties which can keep well until 200 °C as well as good corrosion resistance. The outstanding mechanical properties were mainly attributed to the rigid casting surface layer, grain refinement, grain boundary strengthening obtained by an amount of precipitates as well as solid solution strengthening.

1. Introduction

In recent years, with the fast development of automobile industry, increasing attention has been paid to Mg-based alloys for vehicle weight reduction [1,2]. Most magnesium parts applied to automobiles are high-pressure die-casts mainly due to the high production capacity and relatively low production cost of the die casting process [3,4]. Considering the combination of good die castability with applied mechanical properties, Mg–Al–(Zn)–Mn system has been the basis for almost all present high-pressure die-cast (HPDC) magnesium alloys until now.

Up to the present, the commercial magnesium alloys developed for die-casting applications mainly fall into two classes. The first group is based on Mg–Al and Mg–Al–Zn systems, such as AM50A, AM60B and AZ91D, which have been used for steering wheels, instrument panels and so on. These alloys were developed for the suitable combination of room-temperature strength with ductility, while their application temperature is limited to about 120 °C, above which the mechanical properties decrease sharply [5]. Further investigations have shown that poor elevated-temperature mechanical properties of these alloys are related to the coarsening and softening of discontinuous intermetallic compound β-$Mg_{17}Al_{12}$ phase in the eutectic region and/or the precipitation of the intermetallic compound from supersaturated α-Mg matrix [6]. To further reduce the weight of future vehicle, it is inevitable to expand the use of magnesium to critical components such as transmission and engine parts, which will require these alloys to have much better elevated-temperature properties. Therefore, increasing efforts have been devoted to developing the second group of alloys mainly based on Mg–Al–RE (RE = rare earth), Mg–Al–Si and Mg–Al–Ca/Sr systems, which have improved elevated-temperature performances [7–9]. Because of the formation of relatively thermally stable $Al_{11}RE_3$ phase and the complete suppression of $Mg_{17}Al_{12}$ phase, A HPDC magnesium alloy, AE42 (Mg–4Al–2RE), was developed (by Dow Magnesium) for high-temperature applications [10]. Unfortunately, the decomposition of $Al_{11}RE_3$ phase which leads to the deterioration of creep resistance at temperatures above 150 °C has also been reported [11,12]. Recently, Hydro Magnesium developed a new HPDC alloy, AE44 (Mg–4Al–4RE), whose high temperature mechanical properties was further improved by adding more RE content than AE42 [13]. However, both RE used in AE42 and AE44 are Ce-rich mischmetal, whose typical composition is 52–55 wt.% Ce, 23–25 wt.% La, 16–20 wt.% Nd, and 5–6 wt.% Pr [12], for AE44, the causes of the decline of creep properties at high temperature has not been resolved completely.

* Corresponding author. Tel.: +86 431 85262030; fax: +86 431 85698041.
E-mail address: jmeng@ciac.jl.cn (J. Meng).

0925-8388/$ – see front matter © 2009 Elsevier B.V. All rights reserved.
doi:10.1016/j.jallcom.2009.02.090

Table 1
The chemical compositions of studied alloys (wt.%).

Alloys	Al	Mn	Pr	Mg
AlPr41	4.30	0.35	1.05	Bal.
AlPr42	4.12	0.31	1.95	Bal.
AlPr44	3.89	0.26	3.81	Bal.
AlPr46	4.01	0.32	5.54	Bal.

Since the presence of Al–RE phases play very important roles in affecting the mechanical properties of Mg–Al–RE (AE) series HPDC alloys, its further investigation is necessary and useful for future alloy design, while at present seldom researches have referred to the applications of single Pr element on the HPDC Mg–Al-based alloys. Herein, this work aimed to further investigate about AE alloys and mainly focused on the influences of Pr on the microstructures, mechanical properties and corrosion behavior of HPDC Mg–4Al–0.4Mn alloy.

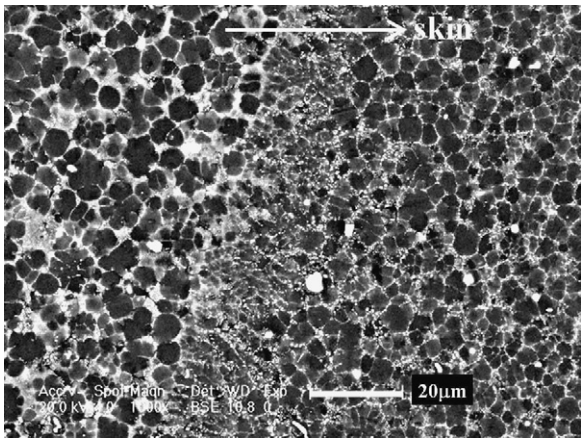

Fig. 2. Typical microstructure of the narrow band in HPDC AlPr46 alloy.

2. Experimental procedure

The nominal compositions of investigated alloys were Mg–4Al–1Pr–0.4Mn, Mg–4Al–2Pr–0.4Mn, Mg–4Al–4Pr–0.4Mn and Mg–4Al–6Pr–0.4Mn and referenced alloy was Mg–4Al–0.4Mn. Commercial pure Mg and Al were used and Mn and Pr were added in the form of Al–10 wt.% Mn and Mg–20 wt.% Pr master alloys. Specimens were die casting using a 280 t clamping force cold chamber die-cast machine. About 20 kg of magnesium alloy ingots were melted in a mild steel crucible. Pure argon was used as a protective gas and refined gas. The metal was hand-ladled into the die casting machine and this required a melt temperature that was about 40 °C higher than that normally used for casting with an automated metering system involving a pump and heated tube, and the melt temperature of 700 °C prior to casting was used. The die was equipped with an oil heating/cooling system and the temperature of the oil heater was set to 210 °C. The chemical compositions of the alloys were determined by inductively coupled plasma atomic emission spectroscopy (ICP-AES) and the results were listed in Table 1, in which the compositions of alloys named as AlPr41, AlPr42, AlPr44 and AlPr46 were given.

The tensile samples were 75 mm in gauge length and 6.1 mm in gauge diameter and the compressive samples were 6.1 mm in diameter and 10 mm in height. Tensile and compressive tests were performed using Instron 5869 tensile testing machine at room temperature (RT) and elevated temperatures with a strain rate of 4.4×10^{-4} s^{-1}. The value in the study was the average of at least four measurements. The hardness of the alloys were measured by Vicker hardness tester, and test load and application time were 25 g and 10 s.

Metallographic samples were cut from the middle segment of the tensile bars and the microstructures of the alloys were observed by scanning electron microscope (SEM) equipped with an energy dispersive X-ray spectrometer (EDS). The specimens for SEM were etched by 4 vol.% nitric acid in alcohol. The average grain size of the alloys was measured by linear intercept method and the analytical system of metallographic image (OLYCIA m3) was used to measure the volume fraction of secondary phase. The phase composition were characterized by X-ray diffraction (XRD). The corrosion specimens were polished successively on finer grades of emery papers up to 800 levels.

Corrosion tests were performed using standard salt spray Corrosion Chamber in neutral 5 wt.% NaCl at different temperatures for 4 days. Cleaning of the specimens in the experiments was done by dipping in a 400 ml aqueous solution of 10%CrO_3 + 1%$AgNO_3$ in boiling condition. The weight loss was measured by an electronic balance with an accuracy of 10^{-4} g. The extent of corrosion was given in weight loss per surface area and time (mg/cm^2/day, or MCD). The reported value was averaged at least three specimens.

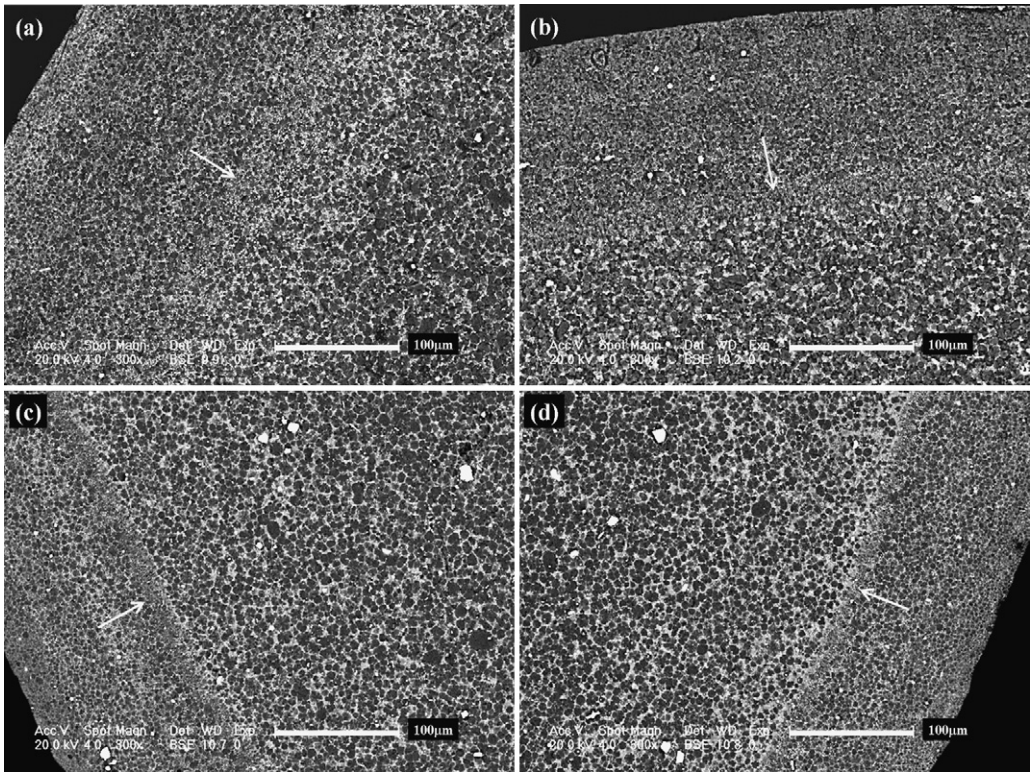

Fig. 1. Low magnification images showing the skin and the partial interior regions: (a) AlPr41, (b) AlPr42, (c) AlPr44 and (d) AlPr46.

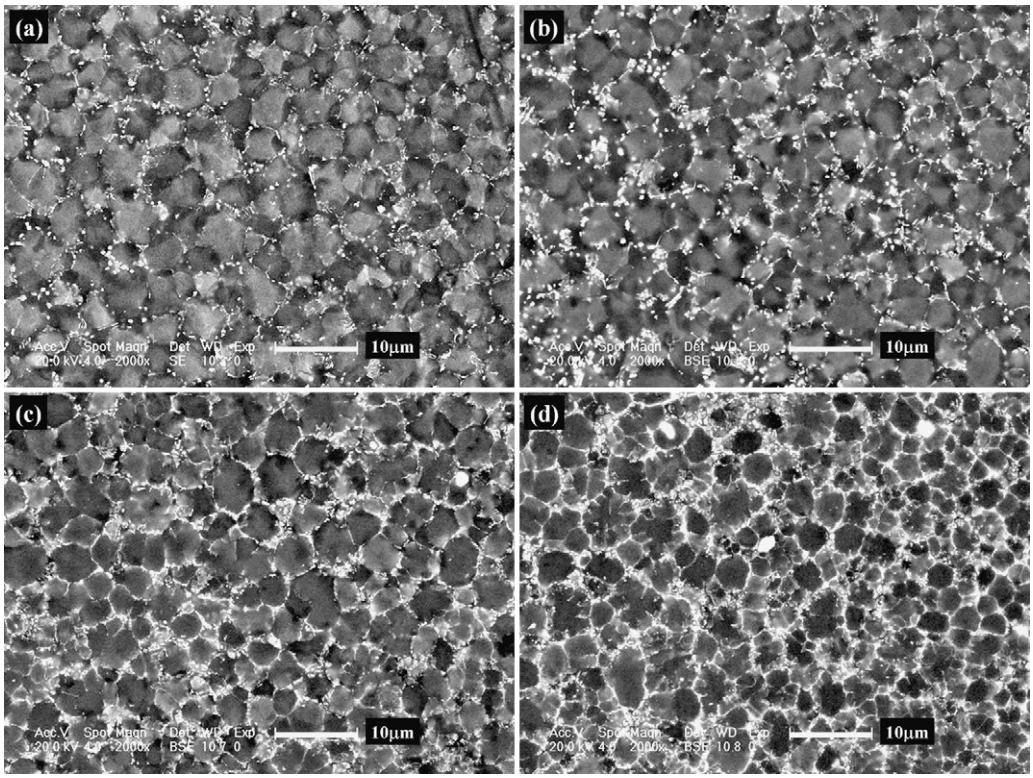

Fig. 3. Microstructures of the skin regions: (a) AlPr41, (b) AlPr42, (c) AlPr44 and (d) AlPr46.

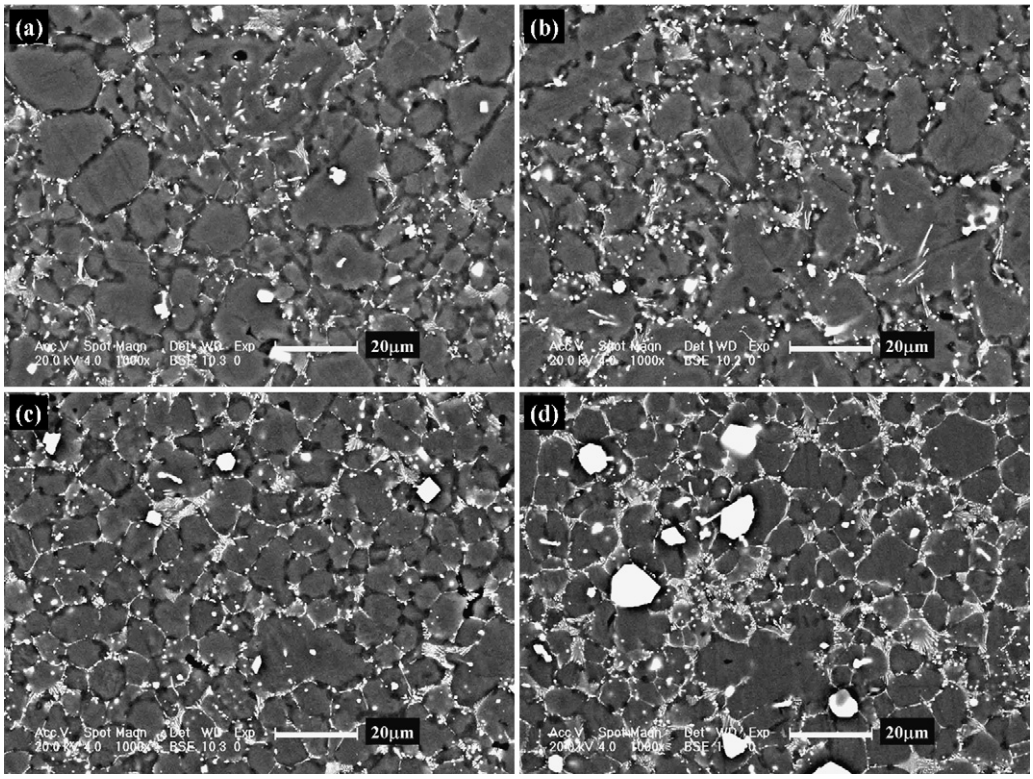

Fig. 4. Microstructures of the core regions: (a) AlPr41, (b) AlPr42, (c) AlPr44 and (d) AlPr46.

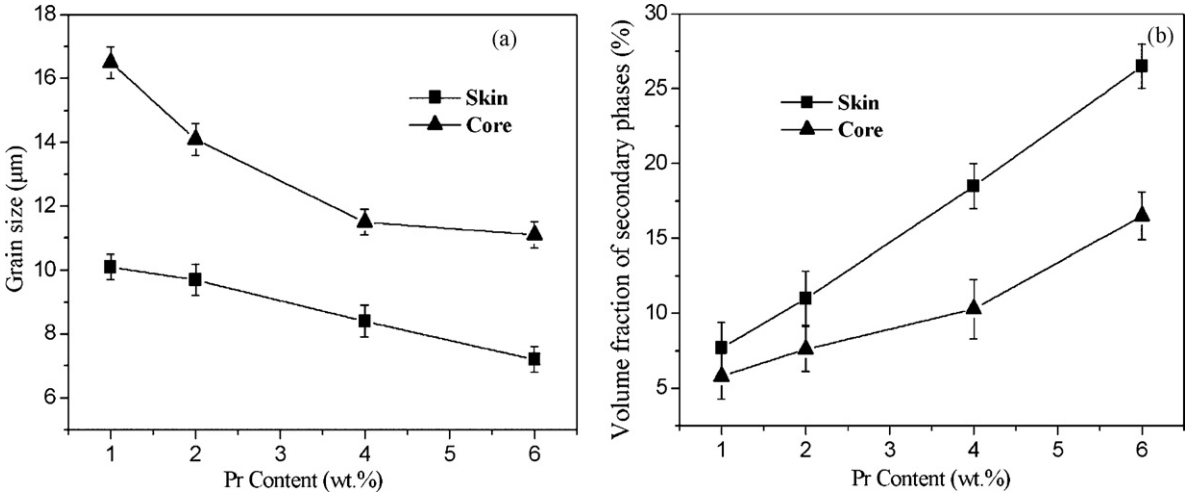

Fig. 5. Effect of Pr content on the grain size and the volume fraction of secondary phases in the skin and the core regions.

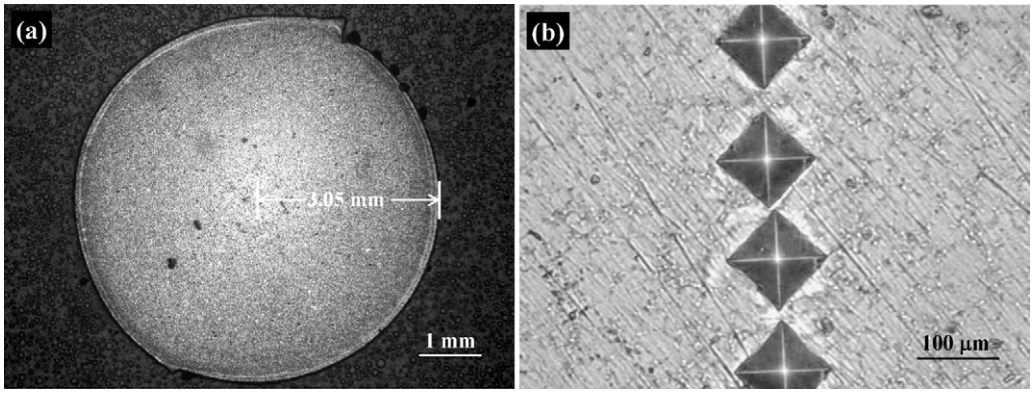

Fig. 6. Typical cross-section of the hardness test (a) and the Vickers indents performed on the sample (b).

3. Results and discussion

3.1. Microstructures

The cross-section microstructures near the surface of the HPDC alloys are shown in Fig. 1. The radius of the cross-section is 6.1 mm. For all the four alloys, a narrow band that follows a contour parallel to the surface of the casting divides the alloy into the skin region and the core region (indicated by arrows), and they seem closer to the casting surface and to be more easily observed with the content of Pr increasing. As a result, the thickness of fine-grained skin decreases from about 200 μm to about 100 μm with the content of Pr increasing from 1.05 wt.% to 5.54 wt.%. Fig. 2 shows the typical microstructure of the narrow band in HPDC AlPr46 alloy. The grains in narrow band were refined obviously compared with that in the neighbouring regions.

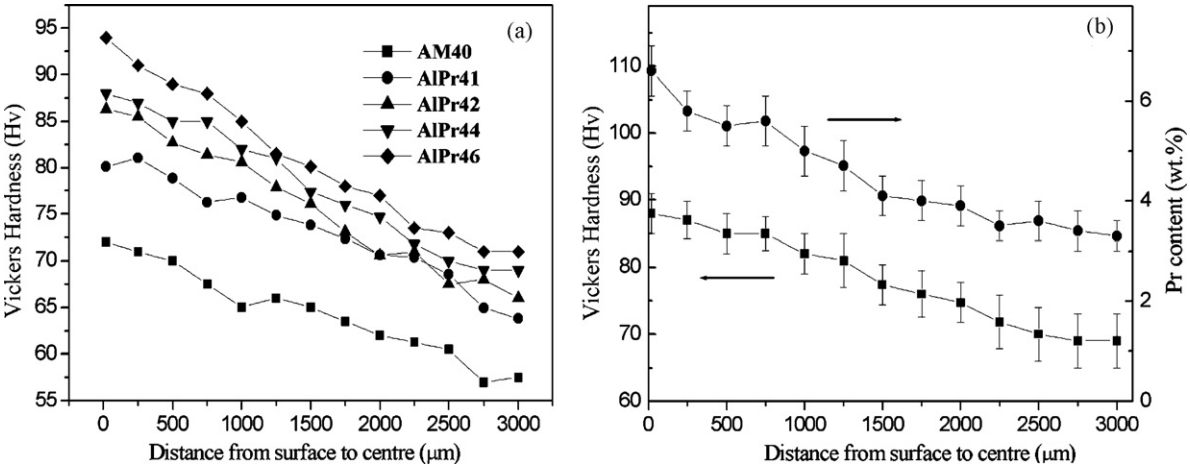

Fig. 7. Variation of the microhardness with the section position for the four studied alloys (a) and Pr content profile of the tensile test bar in HPDC AlPr44 (b) from the surface to the centre.

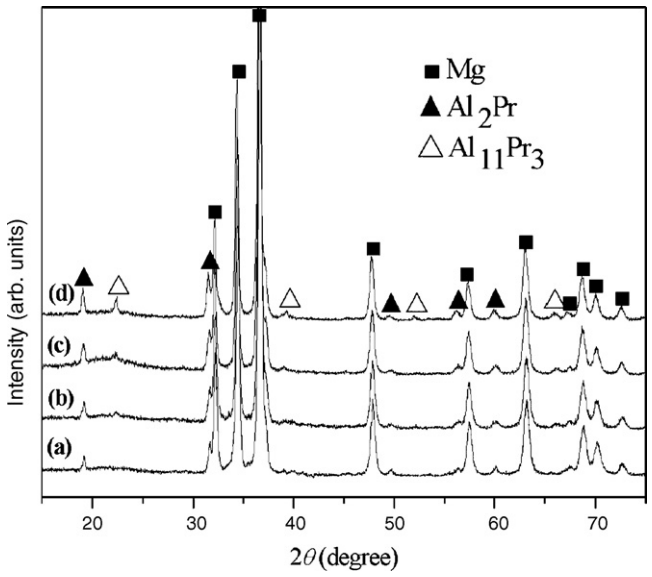

Fig. 8. X-ray diffraction patterns of (a) AlPr41, (b) AlPr42, (c) AlPr44 and (d) AlPr46.

The SEM images of the skin regions and the core regions of the four HPDC alloys are shown in Figs. 3 and 4, respectively. It reveals that all the four alloys are mostly composed of fine equiaxed dendrite and α-Mg solid solution matrix, and an amount of precipitates concentrate near the grain boundaries. The grain size gradually decreases and the volume fraction of secondary phases significantly increases with increasing Pr whether at skin or core regions. Meanwhile, comparing the corresponding images in Figs. 3 and 4, it could be seen clearly that the microstructure of skin region is much finer than that of core region in a same HPDC alloy. For this phenomenon, it is believed that the solidification rate of the skin region is higher as soon as the melted metal reaches the relatively cold mould walls. The specific variation of the grain size and the volume fraction of secondary phases with the increase of Pr content both at the skin regions and the core regions are illustrated in Fig. 5. Moreover, from Figs. 3 and 4 more large particles also could be observed in alloys with relatively high content of Pr, and especially in the core regions the size of some big bulk particles can reach about 10 μm in HPDC AlPr46 alloy. Occasionally, a few large grains could be seen especially in the core region which are derived from the floating crystals in the melted metal, prematurely solidified in the shot sleeve, flow in the die cavity.

The relationship between microhardness and the section position has also been studied in this work. Fig. 6 shows the typical cross-section of the hardness test and the Vickers indents performed on the sample. Fig. 7a shows the variation of the microhardness with the section position for the four studied alloys as well as the reference alloy AM40. It indicates that the hardness decreases obviously from the surface to the center. Meanwhile, it also suggests that in the same location alloys with higher content of Pr have higher hardness. The composition profile of the cross-section is shown in Fig. 7b, which is an example of the variation of Pr content from the surface to the center in HPDC AlPr44 alloy. The general decline of Pr content from the skin to the core is observed. Consequently, we could infer that the high hardness in the skin region is partly related to the high Pr content in the matrix.

3.2. Strengthening phases

XRD patterns of the studied HPDC alloys are illustrated in Fig. 8. It is well known that AM alloys are mainly composed of α-Mg and β-$Mg_{17}Al_{12}$ phases, while as shown in Fig. 8, no obvious peaks of β-$Mg_{17}Al_{12}$ phase emerge in the four alloys as the result of Pr addition. One of the main secondary phases in the four alloys is Al_2Pr phase, and with the Pr content increasing additional characteristic peaks of $Al_{11}Pr_3$ gradually become obvious.

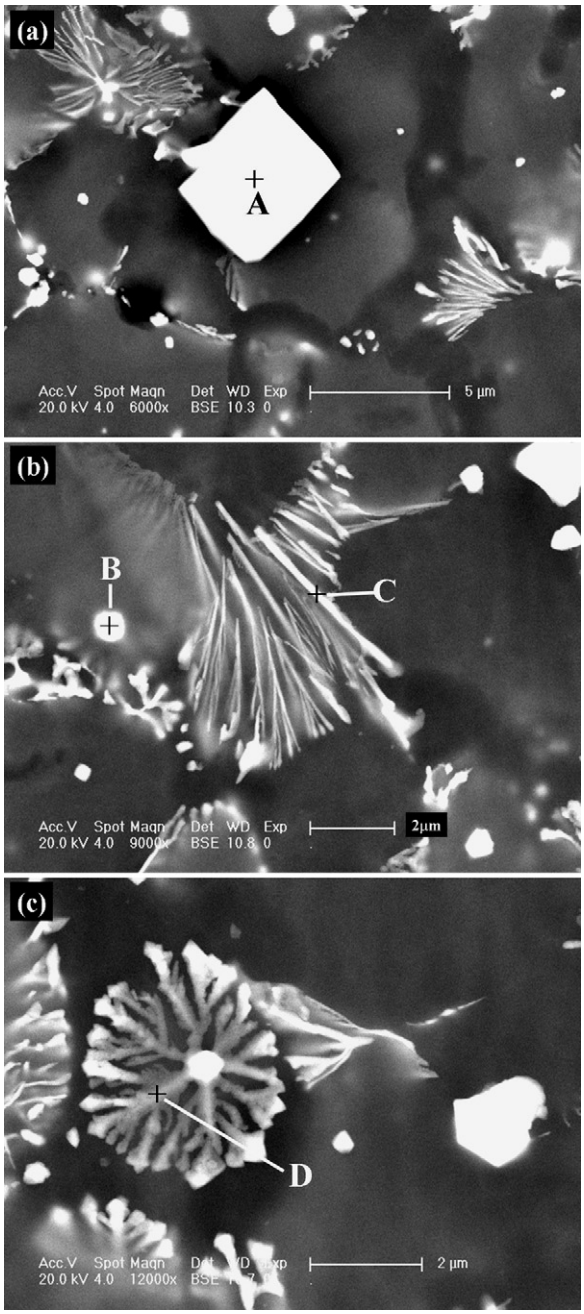

Fig. 9. SEM micrographs of the secondary phases near the grain boundaries in HPDC AlPr44 alloy.

Table 2
The results of EDS analysis of Fig. 9 (The Mg element is wiped off due to no Mg-containing phase detected from the XRD results).

Location	Composition (at.%)			
	n_{Al}	n_{Pr}	n_{Mn}	n_{Al}:n_{Pr}
A	60.46 (1.1)	28.86 (1.7)	1.00 (0.4)	2.09:1
B	7.70 (0.6)	3.62 (0.4)	0.82 (0.3)	2.13:1
C	7.48 (1.0)	1.94 (0.8)	0.06 (0.02)	11.57:3
D	7.45 (1.5)	1.92 (1.3)	0.10 (0.06)	11.64:3

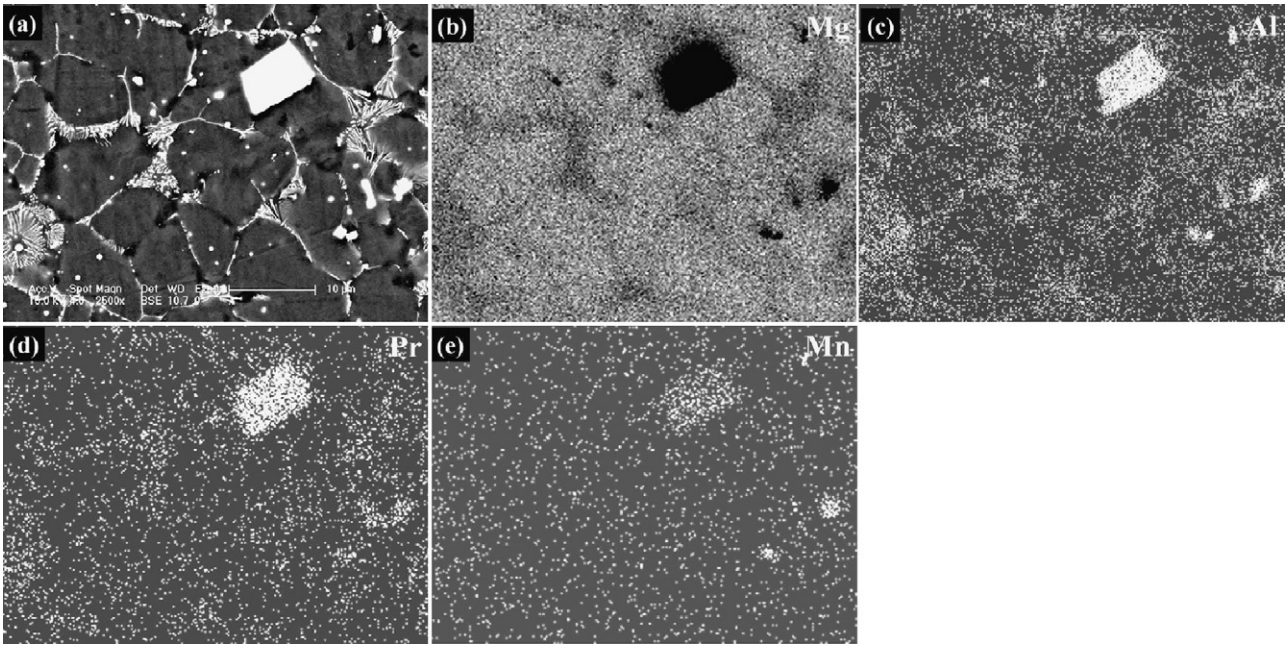

Fig. 10. EDS elemental mapping showing distributions of Mg, Al, Pr and Mn in HPDC AlPr44 alloy.

The further magnified SEM micrographs revealing the secondary phases in the core region in HPDC AlPr44 alloy is shown in Fig. 9. It is evident that the secondary phases mainly comprise four morphologies, marked as A, B, C and D. Each kind of particle was measured at least three times, and the results of EDS analysis of the four points as well as the standard deviation are listed in Table 2. According to the XRD results and Al/Pr ratio, the large quadrangle particle (point A) with size up to 5 μm and the small polygon particle (point B) with size close to hundreds nanometer are both identified to be Al_2Pr phase. The acicular precipitates (point C), approximately 2–5 μm in length and 100–200 nm in diameter, congregate together and are oriented at an angle to the grain boundary direction. In addition, small quantities of petal-like precipitates (point D) with coarse surface distributed near the grain boundaries are also observed. Both the acicular and petal-like precipitates are determined by EDS and XRD analyses to have the chemical formulas $Al_{11}Pr_3$. Map distributions of the elements in HPDC AlPr44 alloy are presented in Fig. 10. It indicates that the alloying element Mn mainly enriches in Al_2Pr phase besides part distribution at the matrix. This analysis result is consistent with the results of EDS microanalyses of the secondary phases shown in Table 2.

3.3. Mechanical properties

Fig. 11 shows the representative stress–strain tensile and compressive curves of HPDC AlPr44 alloy at different testing temperatures. The alloy shows high yield strength and significant strain hardening behavior at RT. Typically, the yield strength and the strain hardening effect decrease when increasing testing temperature, but on the whole, the curves indicate that the mechanical properties of HPDC AlPr44 alloy can keep well until 200 °C. To compare the mechanical properties of the studied alloys, the ultimate tensile strength (UTS), tensile yield strength (TYS) and elongation to failure (ε) from room temperature (RT) to 300 °C are shown in Fig. 12. From Fig. 12a, it is clear that AM40 alloy shows the poorest UTS, while with the addition of Pr, the UTS are significantly improved

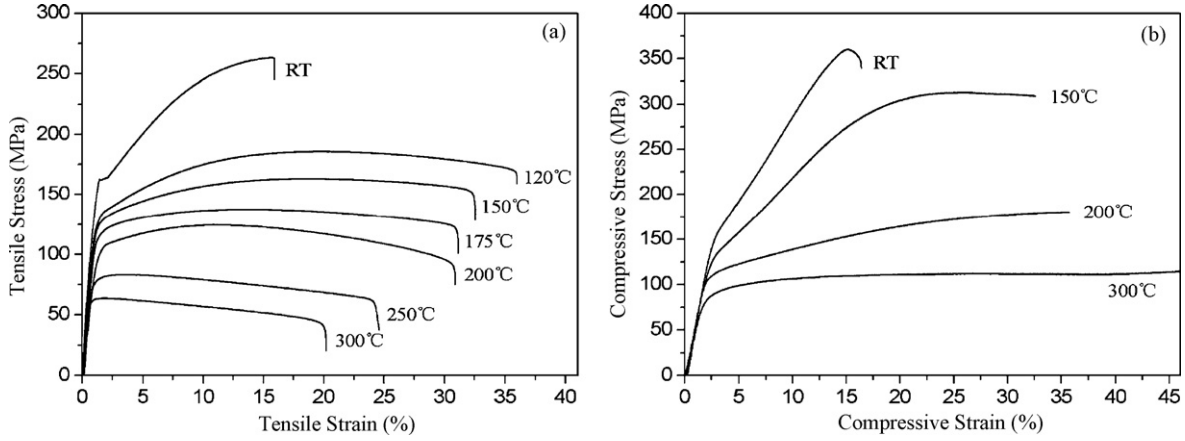

Fig. 11. Typical stress-strain tensile (a) and compressive (b) curves of HPDC AlPr44 alloy at different temperatures.

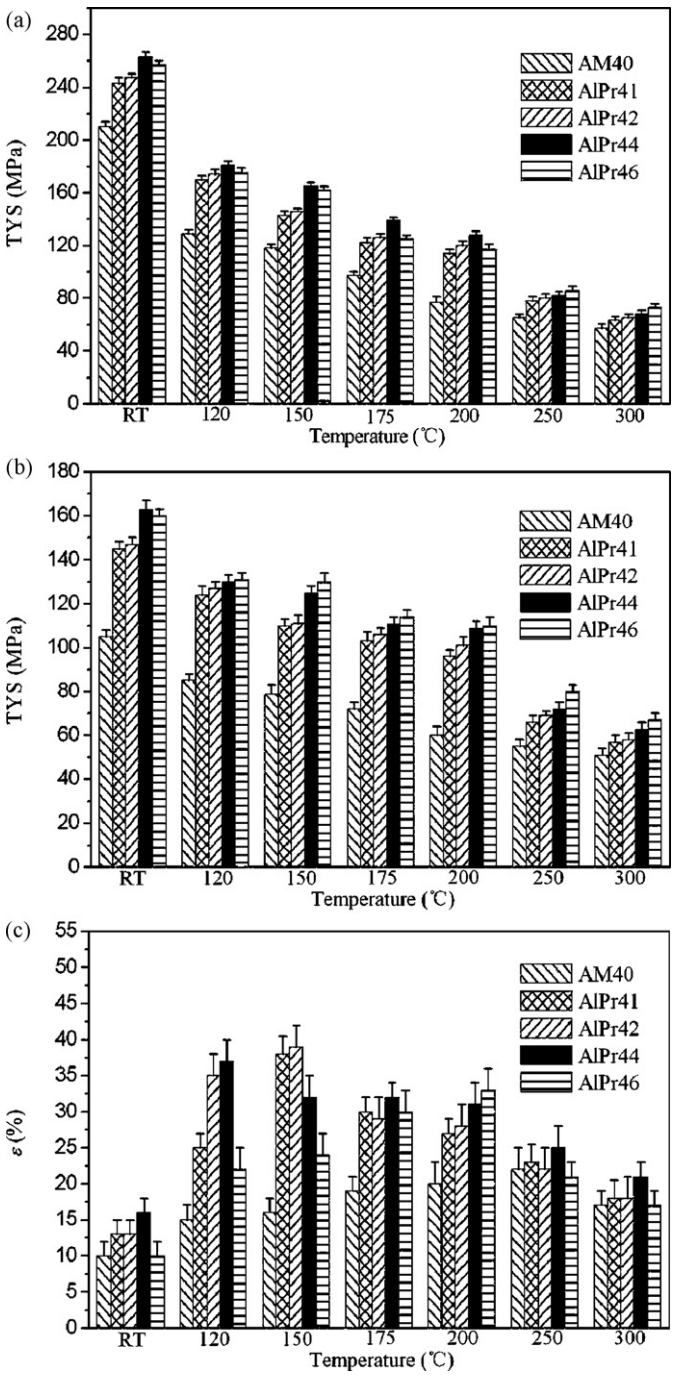

Fig. 12. Tensile properties of the studied alloys at different temperatures.

both at room and elevated temperatures. For example, the UTS of HPDC AM40 alloy are 210 MPa at RT and 77 MPa at 200 °C, while for HPDC AlPr44 alloy, the UTS are 263 MPa at RT, and 128 MPa at 200 °C, respectively. The TYS of the alloys has the general same changing rules with UTS after addition of Pr (Fig. 12b). The highest TYS is obtained from HPDC AlPr44 alloy at RT but at elevated temperatures, the value of AlPr46 is slightly higher than that of AlPr44. For instance, the TYS of HPDC AM40 alloy are 105 MPa at RT and 60 MPa at 200 °C, while the corresponding values for HPDC AlPr44 and AlPr46 alloys are 163 and 160 MPa at RT, and 109 and 111 MPa at 200 °C, respectively. The ductility of the alloys is also improved as the result of Pr addition and at RT the highest value is obtained from HPDC AlPr44 alloy. The elongation of all the alloys studied

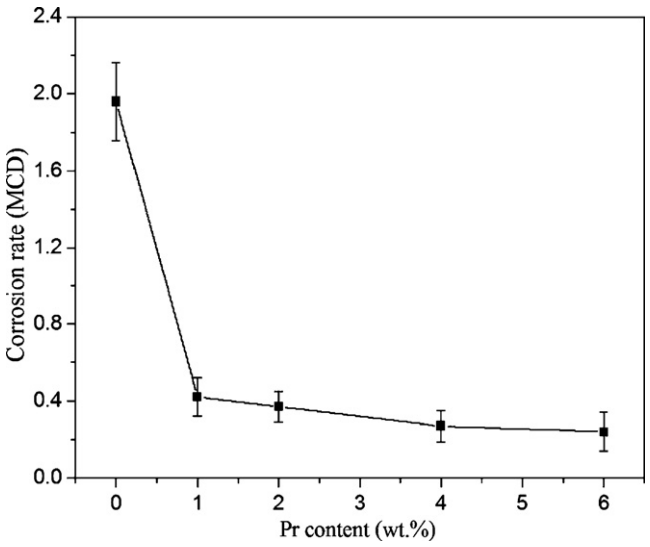

Fig. 13. Weight loss corrosion rates of the HPDC alloys.

increases with the increase of temperature and reaches a highest value at certain elevated temperature (Fig. 12c). Overall evaluation, when the content of Pr is around 4 wt.%, the studied HPDC alloy obtains the optimal mechanical properties.

3.4. Corrosion test

Fig. 13 illustrates the curves of corrosion rates of the HPDC Mg–4Al–0.4Mn–*x*Pr alloys under salt spraying at 35 °C for 4 days. Based on the data, the corrosion resistance of the alloys is improved remarkably due to the addition of Pr and with the increase of Pr content the corrosion rate decreases gradually. The corrosion rate of the best specimen of AlPr46 alloy is below 0.2 MCD. This indicates Mg–Al–Pr series alloys have good salt spray corrosion resistance.

The surface features of the corroded AM40 and AlPr46 alloys after 4 days salt-spray test are presented in Fig. 14. In the case of AM40 alloy, the specimen surfaces suffer corrosion seriously and relatively deep local corrosion pits appear on some areas (Fig. 14a). The amount of large corrosion pits on the specimen surfaces decreases with the addition of Pr. As can be seen from Fig. 14b, there are few large and deep corrosion pits on the surface of AlPr46 alloy. Thus, The surface features of the corroded specimens support the test results of corrosion rates in Fig. 13.

Fig. 15 shows the typical corrosion morphology of AlPr41 and AlPr46 after 4 days salt-spray test. Owing to the long period of salt-spray test (96 h in our study), the corrosion pits could be observed on all the corroded specimens by SEM observation. However, with the increase of Pr content, the pits become smaller and more shallow (Fig. 15). Moreover, it is also found that the corrosion mainly occurs in the interior of the α grains, especially for AlPr46 alloy with high Pr content, which reveals that the grain boundaries are more corrosion resistant.

Fig. 16 shows SEM micrographs of the corrosion products formed on the surfaces of AlPr41 and AlPr46 alloys, respectively. As can be seen from Fig. 16a and b, the corrosion products are composed of voluminous tiny erect flakes. The size of the flakes decreases and the compactness of corrosion film increases with the increase of Pr content. EDS analyses of corrosion product films are revealed in Fig. 16c and d. A small amount of Pr and Al elements are detected in corrosion products of AlPr46 alloy and not discovered in that of AlPr41 alloy. The incorporation of Pr and Al in the brucite layered structure of the film of corrosion product could increase the local positive charge, which is assumed to be balanced by trapped anions

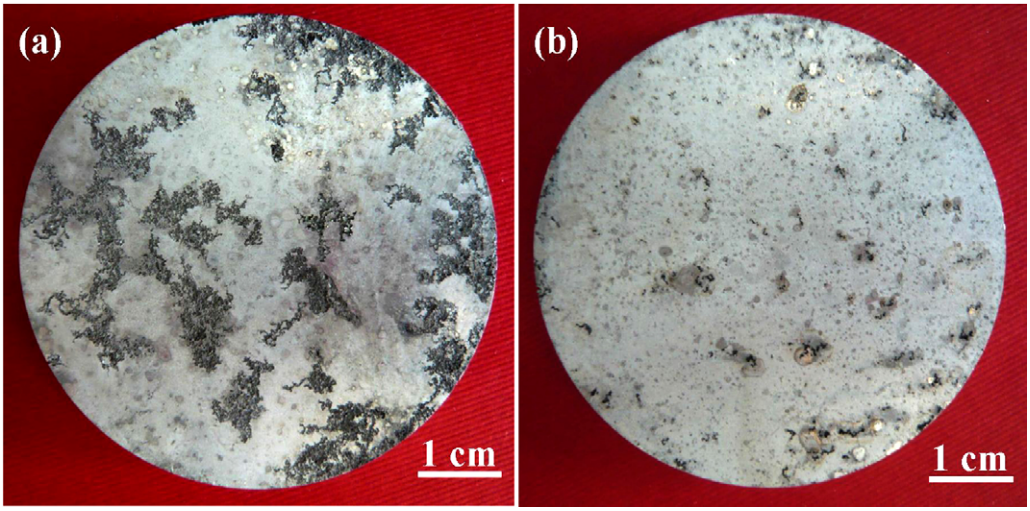

Fig. 14. Macroscopical pictures of the corrosion samples: (a) AM40 and (b) AlPr46.

(such as Cl^-) in the brucite layers, thus further corrosion is inhibited [14].

3.5. Discussion

The results show that the narrow band divides the cross-section into two parts in HPDC Mg–Al–Pr-based alloys. This similar band and the two parts divided by it were also observed in other HPDC Mg alloys [15] as well as HPDC Al alloys [16,17]. In previous literature [15], it has been described that the microstructure characteristics are mainly related to the alloy composition and the casting conditions in HPDC Mg alloys. In the alloys investigated here, solidification during the die-casting process occurs on the die walls as soon as molten metal reaches the relatively cold mould walls and the strong extraction of heat through the walls under the high pressure leads to a rigid casting surface layer, with a very fine microstructure and a higher volume of eutectic. The narrow band is considered to be caused by shear deformation of the semi-solid mush entering the die cavity [15]. Some crystals nucleate and grow in the shot chamber before being injected into the die cavity and they have enough time to grow much larger than the in-cavity solidified grains and are often located at the center of the cross-section in the final microstructure. It is well known that segregation of solid towards the centre of solid–liquid mixtures is a common phenomenon in fluid mechanics [18]. These processes together result in the formation of the microstructure characteristics of HPDC Mg–Al–Pr-based alloys.

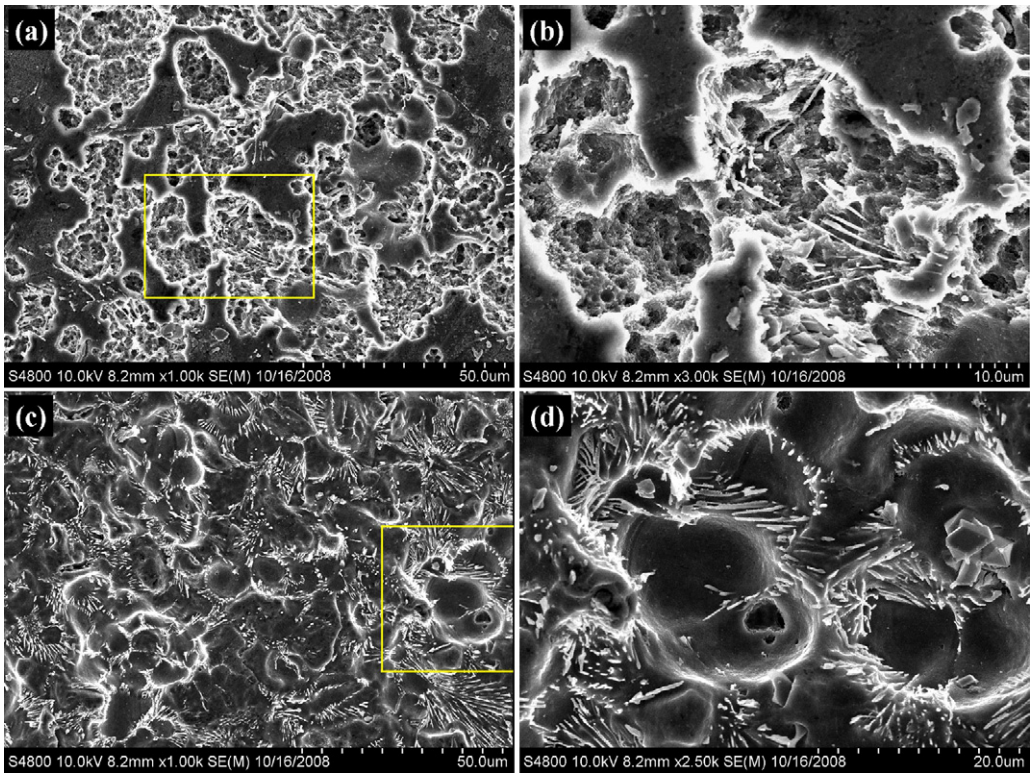

Fig. 15. SEM images of corrosion surface morphology: (a) low and (b) high magnification images of AlPr41 alloy, (c) low and (d) high magnification images of AlPr46 alloy.

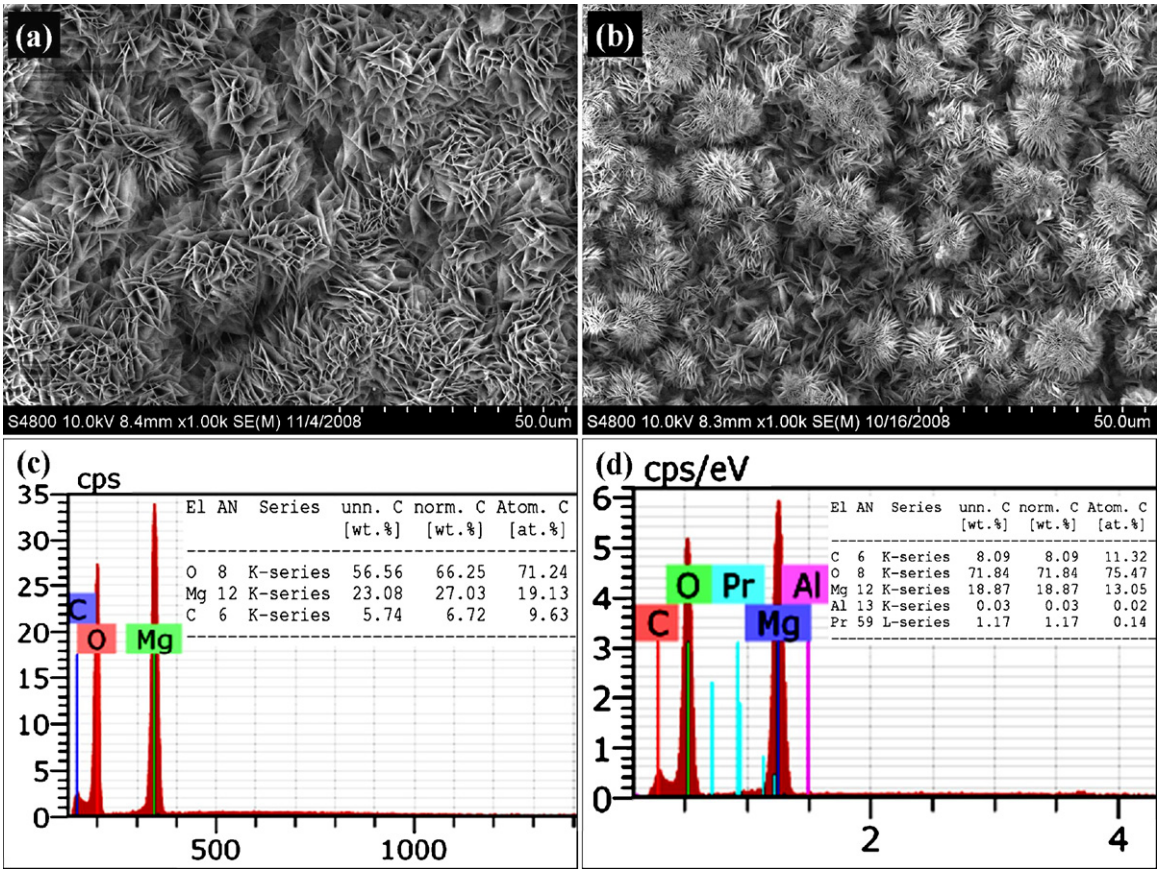

Fig. 16. SEM images of the corrosion products film formed on the surfaces of (a) AlPr41 and (b) AlPr46 alloys, EDS results of corrosion products of (c) AlPr41 and (d) AlPr46 alloys.

Addition of Pr to HPDC Mg–4Al–0.4Mn alloy leads to the complete suppression of $Mg_{17}Al_{12}$ phase formation in the range of tested Pr content, and Pr is combined with Al to form Al–Pr phases as the main secondary phases. The relative volume ratio of Al–Pr phases is found to be related to the Pr content in the alloy. The dominant Al–Pr phase is Al_2Pr when content of Pr is below 4 wt.%, and further addition of Pr leads to the obvious increase of $Al_{11}Pr_3$ phase in volume fraction. The similar rule is also reported in the HPDC Mg–Al–Nd-based alloys [3]. The literatures [19–21] have reported that Al_2RE are formed as a proeutectic phase and $Al_{11}RE_3$ phase is regarded as the product of peritectic reaction:

$$3Al_2RE + L \rightarrow Al_{11}RE_3 \quad (1)$$

According to the above literatures, we infer that there are similar solidification processes in the present alloys. Thus, the reason that formation of $Al_{11}Pr_3$ only goes with high Pr content may be that a high Pr concentration is inclined to accelerate the process of peritectic reaction. Therefore, the $Al_{11}Pr_3$ phase is always found in the grain boundary areas, where Pr content as well as Al content is relatively high.

The HPDC Mg–Al–Pr-based alloys show the high mechanical properties and applied thermal stability at medium–high temperatures. We consider that it is mainly related to the following aspects. Firstly, the results demonstrate that the Pr content in the skin region is higher than that of the core region. Moreover, the microstructure is much finer and more secondary phases concentrate in the

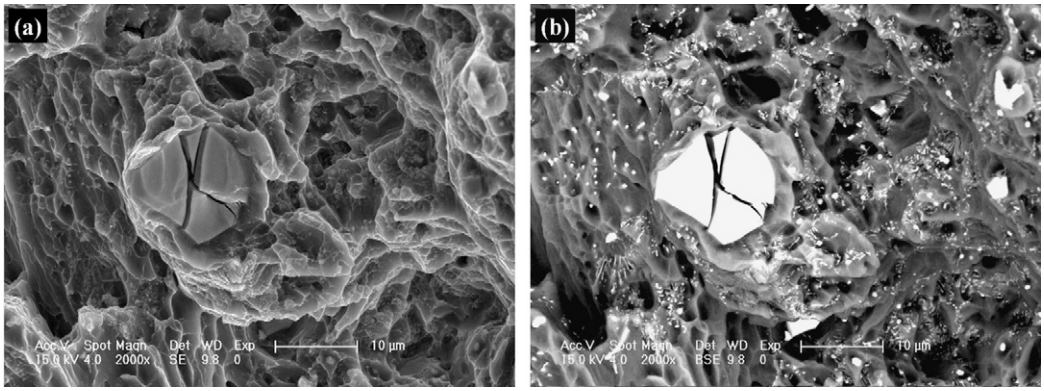

Fig. 17. SEM observations of the big bulk Al_2Pr phase with second cracks on the fracture surface of HPDC AlPr46 alloy: (a) secondary and (b) corresponding backscatter SEM observation.

skin region. Thus, the existence of the rigid cast surface layer plays a positive role in improving the mechanical properties. Secondly, Pr element has higher affinity to Al to suppress the formation of $Mg_{17}Al_{12}$ phase, which is the common secondary phase in Mg–Al-based alloy and has poor thermal stability. At the same time, large amounts of thermally stable Al_2Pr and $Al_{11}Pr_3$ phases form at grain boundary regions, which are considered to be an effective obstacle to grain boundary sliding and dislocation motion in the vicinity of the grain boundaries. Thirdly, the atomic radius of Mg, Al and Pr are 0.160 nm, 0.143 nm and 0.183 nm, respectively [22]. The difference of atomic radius between Mg and Pr is relatively large. Thus Pr atoms dissolving in Mg matrix and replacing the position of Mg result in the more effective aberrance of crystal lattices. Consequently, lattice strain field interactions restrict the movement of dislocation. The last, also a significant effect is the fine grain size due to the addition of Pr, as well as the high-pressure die-casting process. It has been confirmed that the grain boundaries act as a barrier to dislocation motion, namely, a dislocation passing into the near grains of different orientations has to change its direction. Consequently, the strength of alloys can be improved. Meanwhile, generally the grain refinement is also an effective means to improve ductility. However, the HPDC AlPr46 alloy with the minimal grain size does not obtain the best ductility among the alloys studied (Fig. 13c). The reason for this phenomenon may lie in the increasing amount of Al_2Pr particle with large size when increasing the content of Pr, and their cutting effect on the matrix causes the initiation or propagation of cracks. This point can be supported by the fractography of AlPr46 alloy (Fig. 17). Finally, taking into account comprehensively the favorable and unfavorable factors as well as the cost of alloy, we believe that the Pr content added around 4 wt.% in HPDC Mg–4Al-based alloy is suitable to obtain the optimal mechanical properties.

According to the previous studies of Song and Atrens [23,24], the β-$Mg_{17}Al_{12}$ phase in AZ or AM alloys can act as either a corrosion barrier or a galvanic cathode accelerated corrosion. Which role dominates the corrosion process depends on the amount, size and distribution of the β phase. For the Mg–4Al-based alloys containing Pr, the α grains are significantly refined and large amounts of Al–Pr phases concentrating at the grain boundaries separate the α grains, consequently the propagation of corrosion becomes much difficult. Meanwhile, according to Dargusch et al. [25], the potential difference between the second phase containing RE (Al_2RE, $Al_{11}RE_3$, etc.) and the α-Mg is relatively minor, and these Al-RE phases can be passivated in a wide range of pH [26]. Thus the formation of Al–Pr phase would not cause much negative effects coming from micro-galvanic-corrosion. Moreover, the formation of compact corrosion product film containing Pr and Al elements also partly contributes to the low corrosion rate of alloy with high Pr content. The further corrosion mechanism has been under studying. To sum up, the addition of Pr is able to improve the corrosion resistance of Mg–4Al-based alloy remarkably.

4. Conclusions

The structure of high-pressure die-cast Mg–4Al–0.4Mn–*x*Pr (x = 1, 2, 4 and 6 wt.%) alloys are divided into the fine skin region and the relatively coarse centre region by a narrow band, and the microstructures become more refined with increasing addition of Pr. The high hardness in the surface region of the alloy is ascribed to the high cooling rate and the aggregating of alloying elements, such as Pr. The amounts of the secondary phases, Al_2Pr and $Al_{11}Pr_3$ are increased and their relative ratio is changed with the Pr content increasing in the alloy. Considering to the performance-price ratio, the Pr content added around 4 wt.% is suitable to obtain the optimal mechanical properties which can keep well until 200 °C, as well as good corrosion resistance. The outstanding mechanical properties are mainly attributed to the rigid casting surface layer, grain refinement, grain boundary strengthening obtained by an amount of precipitates as well as solid solution strengthening.

Acknowledgements

This project was supported by the Ministry of Science and Technology of China (2006AA03Z520, 2008DFR50160), Chinese Academy of Sciences and Jilin Province. The authors also would like to thank Shanxi Wenxi Yinguang Magnesium Group for their assistance of preparation of samples.

References

[1] M.K. Kulekei, Int. J. Adv. Manuf. Technol. 39 (2008) 851.
[2] T. Laser, Ch. Hartig, M.R. Nurnberg, D. Letzig, R. Bormann, Acta Mater. 56 (2008) 2791.
[3] J.H. Zhang, J. Wang, X. Oiu, D.P. Zhang, Z. Tian, X.D. Niu, D.X. Tang, J. Meng, J. Alloys Compd. 464 (2008) 556.
[4] H. Gjestland, H. Westengen, Adv. Eng. Mater. 9 (2007) 769.
[5] S.D. Sheng, D. Chen, Z.H. Chen, J. Alloys Compd. 470 (2009) L17.
[6] A. Srinivasan, J. Swaminathan, U.T.S. Pillai, K. Guguloth, B.C. Pai, Mater. Sci. Eng. A 485 (2008) 86.
[7] J.H. Zhang, D.P. Zhang, Z. Tian, J. Wang, K. Liu, H.Y. Lu, D.X. Tang, J. Meng, Mater. Sci. Eng. A 489 (2008) 113.
[8] Y. Terada, D. Itoh, T. Sato, Mater. Chem. Phys. 113 (2009) 503.
[9] M.S. Dargusch, S.M. Zhu, J.F. Nie, G.L. Dunlop, Scr. Mater. 60 (2009) 116.
[10] A.A. Luo, Int. Mater. Rev. 49 (2004) 13.
[11] M.O. Pekguleryuz, A. Arslan Kaya, Adv. Eng. Mater. 5 (2003) 866.
[12] B.R. Powell, V. Rezhets, M.P. Balogh, R.A. Waldo, JOM 54 (2002) 34.
[13] P. Bakke, H. Westengen, Magnesium Technol. 12 (2005) 291.
[14] H.B. Yao, Y. Li, A.T.S. Wee, J.S. Pan, J.W. Chai, Appl. Surf. Sci. 173 (2001) 54.
[15] A.K. Dahle, S. Sannes, St.D.H. John, H. Westengen, J. Light Met. 1 (2001) 99.
[16] C.M. Gourlay, H.I. Laukli, A.K. Dahle, Metall. Mater. Trans. A 38 (2007) 1833.
[17] H.I. Laukli, C.M. Gourlay, A.K. Dahle, O. Lohne, Mater. Sci. Eng. A 92 (2005) 413.
[18] P.D. Mccormark, L. Crane, Physical Fluid Dynamics, Academic Press, New York, 1973.
[19] H. Zou, X. Zeng, C. Zhai, W. Ding, Mater. Sci. Eng. A 402 (2005) 412.
[20] H. Zou, X. Zeng, C. Zhai, W. Ding, Mater. Sci. Eng. A 392 (2005) 229.
[21] S.H. Kim, D.H. Kim, N.J. Kim, Mater. Sci. Eng. A 226–228 (1997) 1030.
[22] Y.N. Yu, The Science and Design of Engineering Materials, China Machine Press, 2003, pp. 637–638.
[23] G. Song, A. Atrens, Adv. Eng. Mater. 1 (1999) 11.
[24] G. Song, A. Atrens, Adv. Eng. Mater. 5 (1999) 837.
[25] M.S. Dargusch, G.L. Dunlop, K. Pettersen, in: B.L. Mordike, K.U. Kainer (Eds.), Magnesium Alloys and Their Applications, Werkstoff-Informations GmbH, Wolfsburg, Germany, 1998, pp. 277–282.
[26] G.L. Song, Corrosion and Protection of Magnesium Alloy, Chemical Industry Press, 2006, pp. 169–170.